

Clear-sky infrared aerosol radiative forcing at the surface and the top of the atmosphere

By KRZYSZTOF M. MARKOWICZ¹, PIOTR J. FLATAU^{2,3*}, ANDREW M. VOGELMANN³,
PATRICIA K. QUINN^{4,5} and ELLSWORTH J. WELTON⁶

¹*Institute of Geophysics, Warsaw University, Poland*

²*UCAR Visiting Scientist at Naval Research Laboratory, Monterey, California, USA*

³*Scripps Institution of Oceanography, University of California, San Diego, USA*

⁴*Pacific Marine Environmental Laboratory, NOAA Seattle, Washington, USA*

⁵*Joint Institute for the Study of the Atmosphere and Ocean, University of Washington, USA*

⁶*Goddard Earth Sciences and Technology Center, University of Maryland Baltimore County, USA*

(Received 17 December 2002; revised 10 March 2003)

SUMMARY

We study the aerosol radiative forcing at infrared (IR) wavelengths using data from the Aerosol Characterization Experiment, ACE-Asia, cruise of the National Oceanic and Atmospheric Administration research vessel *Ronald H. Brown*. The analyses apply to the daytime periods of clear-sky conditions for the area within the immediate vicinity of the ship. An optical model is derived from chemical measurements, lidar profiles, and visible-extinction measurements, which are used to estimate the IR aerosol optical thickness and the single-scattering albedo. The IR model results are compared to detailed Fourier transform interferometer-based IR aerosol forcing estimates, pyrometer-based IR downward fluxes, and to observations of the direct aerosol solar forcing. This combined approach attests to the self-consistency of the optical model, and allows us to derive quantities such as the IR forcing at the top of the atmosphere (TOA) and the IR optical thickness. The mean IR aerosol optical thickness at $10\ \mu\text{m}$ is 0.08 and the single-scattering albedo is 0.55. The modelled IR aerosol surface forcing reaches $10\ \text{W m}^{-2}$ during the cruise, which is a significant contribution compared to the total direct aerosol forcing. The surface IR aerosol radiative forcing is between 10 and 25% of the short-wave aerosol forcing. The IR aerosol forcing at the TOA can be up to 19% of the solar aerosol forcing. We show good agreement between TOA aerosol IR forcing derived from the model and from the CERES (Clouds and the Earth's Radiant Energy System) satellite data. Over the Sea of Japan, the average IR aerosol radiative forcing is $4.6\ \text{W m}^{-2}$ at the surface, and $1.5\ \text{W m}^{-2}$ at the TOA. The IR forcing efficiency at the TOA is a strong function of aerosol temperature (which is coupled to vertical structure) and changes between 10 and $18\ \text{W m}^{-2}$ (per IR optical depth unit), while the surface IR forcing efficiency varies between 37 and $55\ \text{W m}^{-2}$ (per IR optical depth unit).

KEYWORDS: Aerosol forcing Aerosol infrared forcing Climate change

1. INTRODUCTION

The effects of sea salt, mineral dust, black carbon, and sulphates in complex environmental conditions are large sources of uncertainty in quantifying regional climate changes (IPCC 2001). Much recent work has been devoted to reducing these uncertainties by mounting major observational campaigns: Smoke, Clouds, and Radiation—Brazil (SCAR-B, Kaufman *et al.* 1998), the Tropospheric Aerosol Radiative Forcing Observational Experiment (TARFOX, Hobbs 1999), the first Aerosol Characterization Experiment (ACE1, Bates *et al.* 1998), ACE2 (Raes *et al.* 2000), the Indian Ocean Experiment (INDOEX, Ramanathan *et al.* 2001), and MINOS (Lelieveld *et al.* 2002), and the Southern African Regional Science Initiative (SAFARI 2002, Swap *et al.* 2002). Thanks to these complementary activities progress has been reported, but this has been limited mostly to the short-wave effects. The infrared (IR) radiative effect of aerosol involves many uncertainties and is usually neglected, despite its potential importance. For example, the modelling study by Lubin *et al.* (2002) showed that the aerosol IR radiative forcing could be as much as 15% of the large, anthropogenic short-wave forcing found over the Arabian Sea during the INDOEX experiment. Modelling studies

* Corresponding author: UCAR Visiting Scientist at Naval Research Laboratory, 7 Grace Hopper Avenue, Monterey, California 93943-5502, USA. e-mail: pflatau@ucsd.edu

indicate that differences in the complicated and highly varied optical properties of mineral aerosols can affect the instantaneous surface IR flux between 7 and 25 W m⁻² (Sokolik *et al.* 1998). Also, global modelling radiative forcing studies indicate that large uncertainties are due to mineral aerosols (Tegen *et al.* 1996; Myhre and Stordal 2001). Direct observations of aerosol IR forcing are rare both at the surface (e.g. Lubin and Simpson 1994; Spänkuch *et al.* 2000) and at the top of the atmosphere (TOA; Ackerman and Chung 1992; Hsu *et al.* 2000). In addition, recent field programmes have provided new observations of aerosol IR effects. During SHADE in the Cape Verde region the Airborne Research Interferometer Evaluation System measured the 8–12 μm signal of a large Saharan dust storm (Highwood *et al.* 2003), clearly showing the direct radiative effect of dust in the atmospheric IR window. Vogelmann *et al.* (2003) observationally surveyed a range of surface aerosol IR radiative forcing encountered during the Aerosol Characterization Experiment in Asia (ACE-Asia). They found that the aerosol IR surface forcing can be significant, with values that can exceed 9 W m⁻² (instantaneous value).

In this work we report a combined modelling and observational study of the IR aerosol optical properties and the direct IR radiative forcing from ACE-Asia. We discuss and compare model results with direct observations of the IR aerosol forcing (Vogelmann *et al.* 2003). The model is tested on the basis of multifaceted observations including surface chemical and optical aerosol properties, columnar and vertical profiles of aerosol optical properties, and surface long-wave and solar radiation fluxes. (Note that we use the term ‘aerosol radiative forcing’ to indicate the radiative effects of any type of aerosol on the fluxes. This is different from another convention within the community, where this term refers only to the changes caused by anthropogenic aerosols.)

2. OBSERVATIONS

The ACE-Asia experiment took place in the spring of 2001 and was designed to study the complex outflow of mineral dust and air pollution from Asia at midlatitudes. The instruments were located on the National Oceanic and Atmospheric Administration (NOAA) research vessel *Ronald H. Brown* which sailed from Honolulu, Hawaii to the Sea of Japan. On the Pacific transect we were able to observe passages of extratropical cyclones and long-range pollution transport. The sampling near the Asian coast found both pollution and dust from the arid regions of Asia.

The total IR radiative fluxes (3.5–50 μm) were obtained using the broadband, hemispheric view, precision IR radiometer pyrgeometer (PIR; Eppley Laboratory, Rhode Island, USA). According to the technical specifications provided by the manufacturer, this instrument has an absolute accuracy of ±2%. Two handheld Microtops II (sunphotometer and ozonometer, Morys *et al.* 2001) with spectral filters for visible and near-IR wavelengths were used to retrieve the aerosol optical thickness (AOT), columnar water vapour, and columnar ozone. The AOT was measured at 380, 440, 500, 675, 870 nm by the sunphotometer and at 1020 nm by the ozonometer. The total-water column was obtained from the sun radiance measured at 936 and 1020 nm. The Microtops instruments were calibrated at the Mauna Loa Observatory, Hawaii, just after the field phase of ACE-Asia, and the data were post-processed using the new calibration constants. The absolute accuracy of these instruments is about 2%, but the error in the derived total optical thickness is largest for a low air mass (near solar noon). Therefore, the accuracy of the AOT is about 0.02 at 500 nm.

A Fourier Transform IR (FTIR) radiometer measured the sky radiance during the cruise, and its design is based on the Atmospheric Emitted Radiance Interferometer

(AERI, Revercomb *et al.* 1988). The Marine-AERI (M-AERI) measures the sky radiance from 520 to 3020 cm^{-1} (about 18 to 3 μm) at $\sim 0.5 \text{ cm}^{-1}$ resolution. Vogelmann *et al.* (2003) used these spectra to determine the IR aerosol forcing in the 10 μm window, and these observations are used here to test our aerosol IR model. Such high-resolution spectra provide certain advantages for determining aerosol IR effects (e.g. discussed by Vogelmann *et al.* (2003)), which is why FTIR spectra have been used for such studies despite their complexity (Lubin and Simpson 1994; Spänkuch *et al.* 2000; Highwood *et al.* 2003).

Vertical profiles of the aerosol extinction coefficient at 523 nm were measured by a micropulse lidar (MPL, Welton *et al.* 2000). The vertical resolution of this instrument is 75 m. The aerosol extinction coefficient profile was obtained from the calibrated lidar signal assuming an altitude-independent ratio of backscatter to extinction. NOAA's Pacific Marine Environmental Laboratory determined the concentrations of chemical components in the submicron and supermicron size ranges. The analysed components include sea salt, sulphate, nitrate, total organic carbon, elemental carbon, and dust. 'Submicron' and 'supermicron' refer to all particles with aerodynamic diameters less than 1 μm and between 1 and 10 μm , respectively, at 55% relative humidity (RH). The methodology of the chemical analysis is described elsewhere (cf. Quinn *et al.* 2001, 2002). We divided the chemical species into several groups according to their physical properties: sulphate and nitrate aerosol mass, sea salt mass, total organic carbon, elemental carbon, and dust. The concentration of dust was derived assuming that all elements were in their common oxide form (Malm *et al.* 1994). The particulate organic matter (POM) was determined from the measured organic carbon (OC) concentration and the expression $\text{POM} = 2.1 \times \text{OC } \mu\text{g C m}^{-3}$ (Turpin and Lim 2001). On the basis of these mass concentrations, we associated the optical properties with these chemical components. Clearly, only surface chemical measurements were available to us directly, and values above the surface were approximated by extrapolation. However, lidar data and a numerical transport model provide additional information on the vertical profile of the dust, which is a major contributor to the IR signal. The combined accuracy of these approximations will be tested on the basis of comparison with the FTIR data.

The TOA IR fluxes were obtained from the Clouds and the Earth's Radiant Energy System (CERES) satellite instrument on board the TERRA satellite (the resolution of CERES is 20 km at nadir). CERES measures radiances, which are converted to fluxes using angular-distribution models (Loeb and Kato 2002). In this study we use Beta 2 single scanner footprint (SSF) CERES data.

3. AEROSOL MODEL

The IR radiative aerosol forcing is obtained from radiative-transfer calculations (MODTRAN version 4.1, Anderson *et al.* 2001). We use an aerosol optical model based on chemical measurements. We developed a new optical aerosol properties model that offers more flexibility than the Optical Properties of Aerosols and Clouds, Global Aerosol Data Set (OPAC/GADS) software which was used previously (Markowicz *et al.* 2003). In short, the current version offers the advantage that the optical properties such as extinction, absorption coefficient, and the asymmetry parameter are recalculated from Mie theory (Bohren and Huffman 1983), rather than taken from fixed tables, and the choice of size-distribution parameters is more flexible. We define seven aerosol types: water-soluble, soot, sea salt accumulation and coarse modes, mineral dust accumulation and coarse modes, and sulphate. The 'soluble' categories are: (a) nitrate and POM, and (b) sulphates (they differ because different humidity growth factors are assumed).

TABLE 1. MODE RADIUS (r_m) AND WIDTH σ OF THE LOG-NORMAL SIZE DISTRIBUTION IN μM

	Sea salt		Dust		Sulphate		
	Soluble	Soot	Fine	Coarse			
r_m	0.03–0.075	0.011	0.10	1.75	0.15	1.9	0.02–0.1
σ	2.24	2.00	2.03	2.03	1.95	2.15	2.03

The soot category includes elemental carbon. The mass of the dust category is defined as:

$$\text{Mass} = 2.2 \text{ Al} + 2.49 \text{ Si} + 1.63 \text{ Ca} + 2.42 \text{ Fe} + 1.94 \text{ Ti}$$

with numerical factors adjusted such that the major elements in dust are converted to their common oxide form (Malm *et al.* 1994).

We assume that the aerosol components are an external mixture and we perform the Mie computations separately for all seven types of aerosols. The refractive index of aerosols between 0.25 and 40 μm was obtained from the Optical Properties of Aerosol and Clouds software (OPAC 3.1, Hess *et al.* 1998) and the HITRAN* (HAWKS 2000, Rothman *et al.* 1998) aerosol information. To account for water vapour intake, the complex refractive index of the medium must be modified by mixing it with the refractive index of water. The effective refractive index for the hygroscopic type of aerosols (soluble and sea salt) are obtained from the Maxwell–Garnett mixing rule (Chylek *et al.* 1988).

We used a log-normal size distribution to describe the particle optical properties. The soluble, soot, and sulphate types of aerosols (which are generally small) are defined by one single log-normal size distribution. The sea salt and dust particles are described by two log-normal size distributions (accumulation and coarse mode). However, we have aerosol mass density measurements for both submicron (radius $r < 0.5 \mu\text{m}$) and supermicron ($0.5 \mu\text{m} \leq r \leq 5.0 \mu\text{m}$) particles. In the case of a single mode (assumed) distribution, we calculate the equivalent mode radius (Table 1) and number of particles on the basis of these two measured masses and the assumed width of the size distribution (σ) from the OPAC/GADS data base (Table 1). For sea salt and dust, we use two log-normal distributions and have to assume the mode radius for the fine and coarse fractions (Table 1) to calculate the number of particles from the submicron and supermicron mass measurements.

For the given dry aerosol mass density ($\mu\text{g m}^{-3}$) in each category, we assume a growth factor (Hanel and Zankl 1979) and calculate the aerosol mode radius at 55% RH. It is this modified radius that is used to define masses in accumulation and coarse modes. In summary, we obtain the number of particles and mode radii for all seven types of aerosol.

The aerosol chemical composition is assumed to be constant with altitude to 3 km, but the vertical optical properties change with height due to the humidity variation. In the upper layer (above 3 km) the aerosol optical model includes only dust particles. This is consistent with the numerical simulations performed by the Coupled Ocean Atmosphere Mesoscale Prediction System (COAMPS)/Navy Transport Model and the MPL lidar observations, which show layered dust structure for year day 99 (YD99) onwards. The optical thickness and vertical structure of these two layers were obtained from the MPL lidar measurements at 523 nm. The spectral extinction coefficient, single-scattering albedo, and asymmetry parameter at 62 wavelengths were calculated for these

* HITRAN is the high-resolution molecular absorption database.

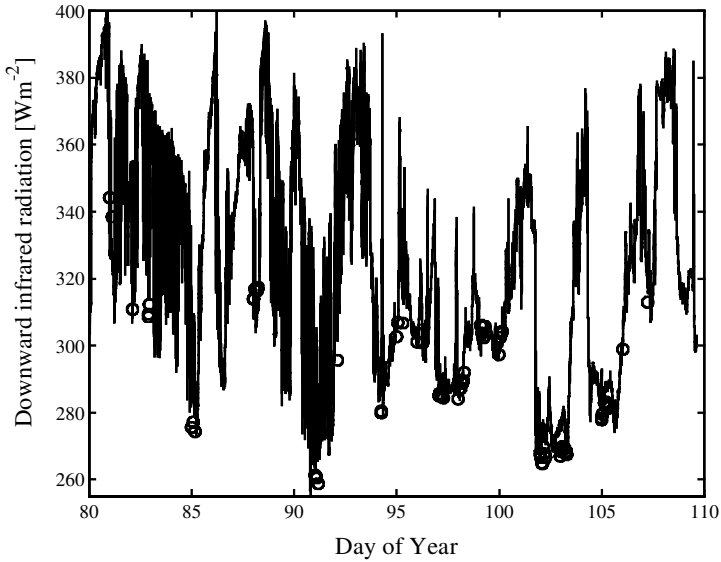


Figure 1. Downward long-wave flux ($3.5\text{--}50\ \mu\text{m}$) at the surface as a function of year day. The solid line represents pyrgometer observations and the open circles mark model results.

two layers using our optical properties package described above. From the vertical profile of RH (atmospheric soundings from the ship were available approximately every 3 hours) and the lidar profiles of aerosol optical thickness, we define the mean RH in the two layers. These spectral optical properties were used in the radiative-transfer model calculation. It must be stressed that the refractive index used was not measured and is based on the OPAC database. Also, we did not use the size-distribution data at the surface, even though they were available. We opted to keep the model simple but compared the results with detailed measurements, a point which we will discuss further. In this respect, the contribution by Highwood *et al.* (2003) is much more comprehensive.

4. RESULTS

(a) Broadband fluxes

Radiative-transfer calculations are based on: chemical measurements, lidar extinction observations, atmospheric soundings, Microtops aerosol optical thickness (AOT) data, and columnar ozone. We performed model calculations for 81 cases corresponding to the Microtops observations. All of the AOT measurements were performed under clear-sky conditions, although small cloud fraction is possible outside the solar aureole. The cloud fraction was determined from the whole-sky imager (not reported here). Both the Microtops and the FTIR measurements are not affected by the small cloud fraction out of the field of view. However, the hemispherical measurements such as pyrgometer are sensitive to such clouds. This point is discussed next.

Figure 1 shows the downward long-wave radiation ($3.5\text{--}50\ \mu\text{m}$) at the surface during the cruise. High values of fluxes are correlated with the cloudy conditions and large RH. Notice that the model results define the minimal envelope of the pyrgometer observations associated with the clear-sky conditions. For example, after the stormy night on YD85, we measured visible AOT as high as 0.45 (at $0.5\ \mu\text{m}$) which correlates with a small long-wave flux ($275\text{--}285\ \text{W m}^{-2}$), indicating clear-sky conditions.

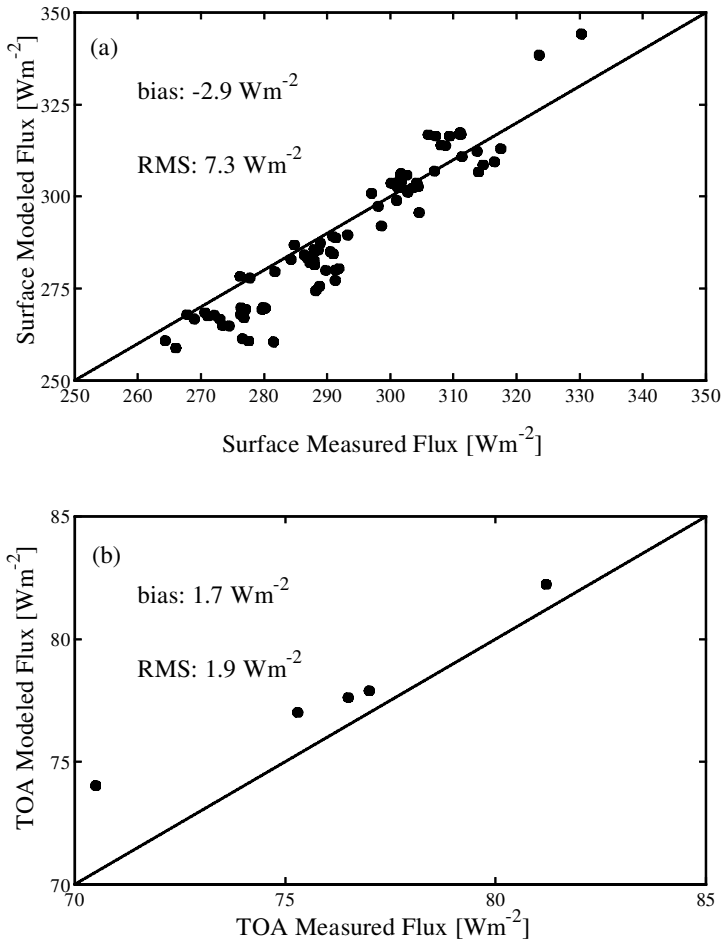


Figure 2. Comparison of measured and modelled: (a) downward long-wave fluxes between 3.5 and $50 \mu\text{m}$ at the surface, and (b) outgoing fluxes in the atmospheric window ($8\text{--}12 \mu\text{m}$) at the top of atmosphere (TOA).

The agreement between the model and the pyrgeometer is better quantified in Fig. 2(a), which shows that the radiative-transfer model underestimates the total downward fluxes by 2.9 W m^{-2} . In spite of a relatively large r.m.s. (7.3 W m^{-2}), the modelled fluxes can be considered in good agreement with the measurements. The total columnar water significantly influences the difference between observations and model results, partially because soundings were only available, at best, every 3 hours (no attempt was made to use FTIR retrieved soundings in this work). Because of these issues and potential cloud presence, we do not use the pyrgeometer to derive IR forcing.

We used the CERES observations (on the TERRA satellite) to compare fluxes at the TOA. The satellite observation footprint and ship position were collocated with a maximum deviation of 25 km. We chose only data for which the viewing angle was less than 60 degrees. Figure 2(b) shows a comparison of the TOA modelled and CERES outgoing long-wave flux in the atmospheric window ($8\text{--}12 \mu\text{m}$). We have only five such days with the cloud-free conditions. For the TOA the model overestimated the satellite data by 1.7 W m^{-2} . The difference between model and observations is positive and has a small r.m.s. (1.9 W m^{-2}). Possible error sources are the angular-distribution model

specifications (Loeb and Kato 2002), which are used to convert radiances to fluxes in the SSF CERES data, and uncertainties in the aerosol optical model specifications. Model calculations of fluxes in the atmospheric window at the TOA show that the outgoing long-wave flux is largely independent of the total column water vapour and, therefore, the TOA flux from CERES can be used to estimate the IR aerosol forcing.

(b) *The infrared aerosol optical properties*

In this section we consider the IR radiation in the atmospheric window between 8–12 μm . As usual, aerosol properties depend on the refractive index and the aerosol size distribution. The coarse-mode particles ($r > 0.5 \mu\text{m}$) can effectively scatter or absorb long-wave radiation. For these particles their single-scattering properties are determined by the transition between the Rayleigh and Mie regimes (size parameter $x > 0.3$). Because the extinction efficiency is small for $x \approx 0.3$, and because there are not many large aerosol particles, the IR extinction is small in comparison to the visible extinction at 500 nm. During ACE-Asia the number of particles in the sea salt coarse mode varied between 0.005 and 0.38 cm^{-3} and the number of dust particles in coarse mode varied between 0.01 and 0.63 cm^{-3} (remember that these are derived concentrations, and can possibly contain contributions from various errors).

We obtained the aerosol optical properties in the IR atmospheric window using the aerosol optical model, the vertical profile of extinction coefficient from MPL lidar observations, and the aerosol optical thickness at 500 nm. Figure 3(a) shows a high temporal variation of the IR aerosol optical thickness during the cruise. The mean value of the IR AOT is 0.08 (± 0.07) and it is 20% of the AOT observed at 500 nm (Markowicz *et al.* 2003). Lower values of the IR AOT (between 0.03 and 0.05) in the first part of the cruise were associated with the clean marine air masses of the central and western Pacific Ocean. Only during YD85, after a frontal passage, did the IR AOT increase to about 0.18 in the morning and 0.13 later that afternoon. The ratio of visible to IR AOT was approximately 2.5, which is relatively small due to the increase in concentration of large particles. For that case we observed a flat spectral AOT (small Ångström exponent) from the visible to the near-IR. The Ångström exponent evaluated for 500 and 870 nm is shown in Fig. 4(a) for the ACE-Asia cruise. Small values over the central Pacific Ocean correspond to clean marine air masses with a small fraction of submicron particles; large values correspond to a large presence of submicron particles, especially those associated with pollution. Between YD97 and YD103, a mineral dust aloft had significant influence on the optical properties of aerosol as seen by the small Ångström exponent.

Between YD98 and YD99 the IR AOT increased strongly, which correlates with the presence of dust layers in the middle troposphere. Throughout YD99 the IR AOT was 0.25 while the visible value was about unity. From YD99 onwards, the layer of dust was descending and on YD102 the situation was dominated by dust in the boundary layer. The number of dust particles in the coarse mode inferred from chemical measurements at the surface was about 0.6 cm^{-3} . The IR AOT was 0.15 in the morning, and decreased to 0.1 later that afternoon. These results correlate with the visible AOT and the dust concentration at the surface. During the last days of the cruise, the IR AOT was small, with the exception of YD107 when it increased to 0.13.

The variability of the no-dust IR optical thickness (Fig. 3(a)) was much smaller than the total IR optical thickness, usually being smaller than 0.05 with the exception of YD85. During the days with dust, it contributed about 20% to the total IR optical thickness.

Overall the correlation coefficient between the IR AOT and visible (500 nm) AOT is 0.82 (Fig. 4(b)). Despite the significant correlation, we cannot estimate the IR AOT

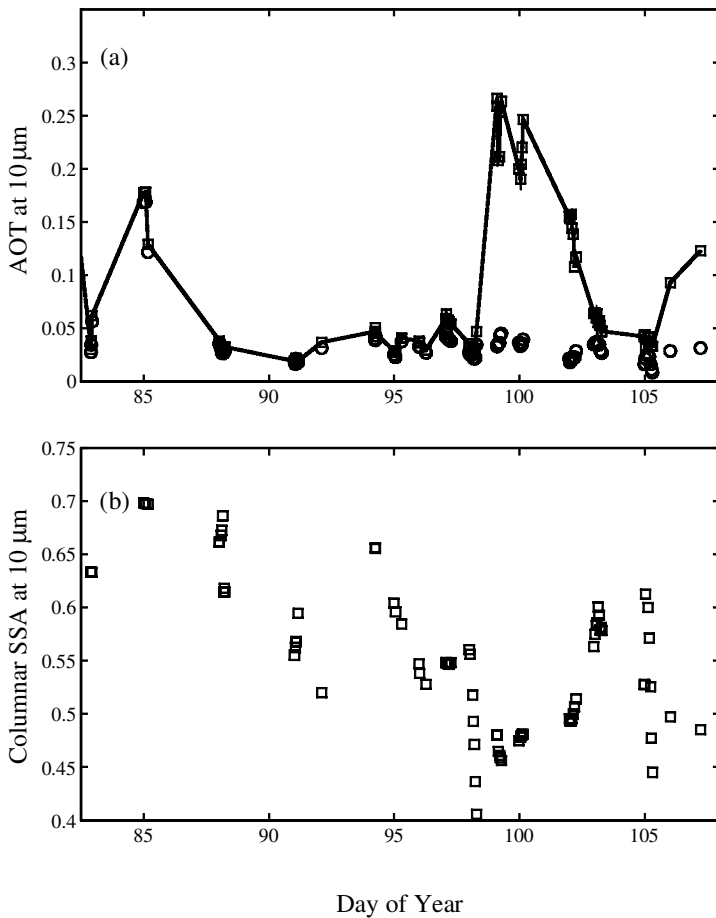


Figure 3. Temporal variation of: (a) total (open squares and solid line) and no-dust (open circles) infrared (IR) aerosol optical thickness (AOT) at $10\ \mu\text{m}$, and (b) vertically averaged infrared single scattering albedo (SSA) at $10\ \mu\text{m}$ during the Aerosol Characterization Experiment, ACE-Asia, cruise.

based on a single visible, spectral measurement. However, the multi-spectral observations by the sunphotometer include information about columnar size distribution. For example, the Ångström exponent, defined for two wavelengths, is a function of the ratio of the particle concentration in the accumulation to that in the coarse mode. Therefore during days with high-IR AOT, we measured low values of the Ångström exponent. Moreover during these days, correlation of the IR AOT and visible AOT is much better (Fig. 4(b)).

The columnar IR single-scattering albedo (SSA) at $10\ \mu\text{m}$, defined here as the extinction-weighted SSA, is shown in Fig. 3(b). The SSA varies from 0.4 to 0.7; thus the scattering of radiation in the atmospheric window is appreciable. The highest values of the SSA (0.65–0.7) were observed in the first part of the cruise and correspond to an almost conservative SSA in the visible. The correlation (R) between visible and IR SSA is poor ($R^2 = 0.66$) although the general trend of these two quantities (not presented) is similar. One important reason for such a small correlation is the presence of water vapour. In the visible, an increase in RH leads to an increase of SSA, while in the IR atmospheric window the imaginary part of the refractive index of water is large and an

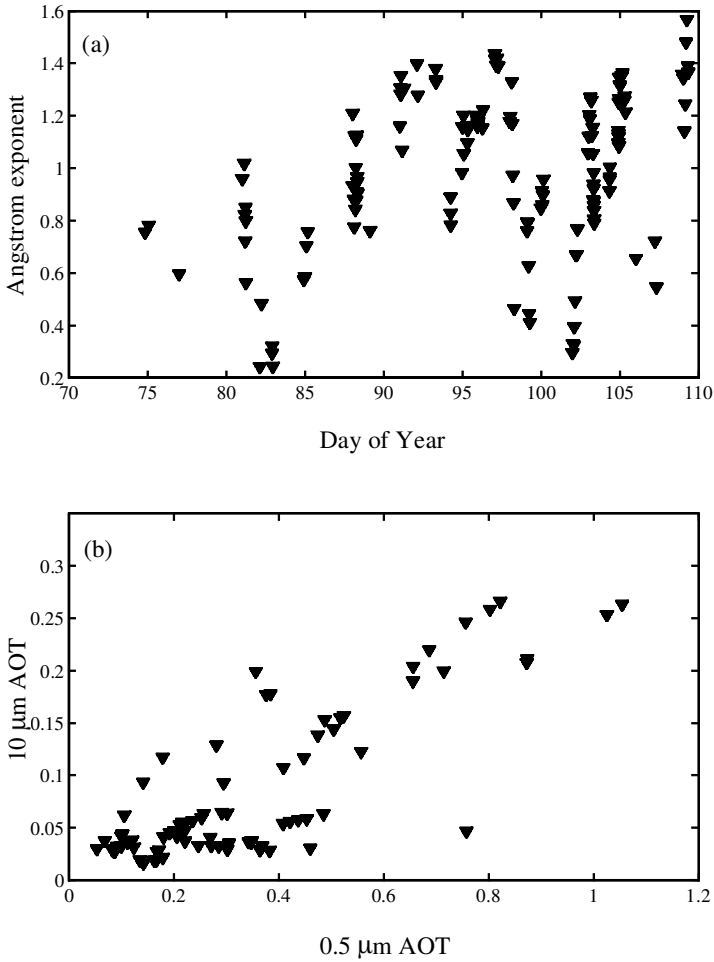


Figure 4. (a) Ångstrom exponent plotted against year day, and (b) infrared (at $10\ \mu\text{m}$) aerosol optical thickness (AOT) as a function of the visible (at $0.5\ \mu\text{m}$) AOT.

increase in RH correlates with an increase of absorption (smaller SSA). Over the Sea of Japan, the IR SSA is smaller in comparison to the Pacific transect, and during the dust events the IR SSA is between 0.45 and 0.5.

There were no direct measurements of the SSA in the IR. However, the measured surface SSA at 550 nm compares well with the modelling results in the visible (Markowicz *et al.* 2003), which provides a certain degree of confidence about the validity of our optical model. The aerosol refractive index and size distribution of particles are the sources of uncertainty in derivation of the IR SSA. This is particularly true about mineral dust. The mineral dust refractive index changes significantly with its composition (Sokolik *et al.* 1998). However, in this study we used the refractive index of dust available in the OPAC/GADS database. We test our optical model against available measurements of extensive parameters (fluxes). Also, the size-distribution changes lead to large changes of the IR SSA. Figure 5 shows SSA as a function of a size parameter ($x = 2\pi r/\lambda$) based on the effective radius. The three lines on this figure correspond to different imaginary parts (k) of the refractive index. The dotted line corresponds to

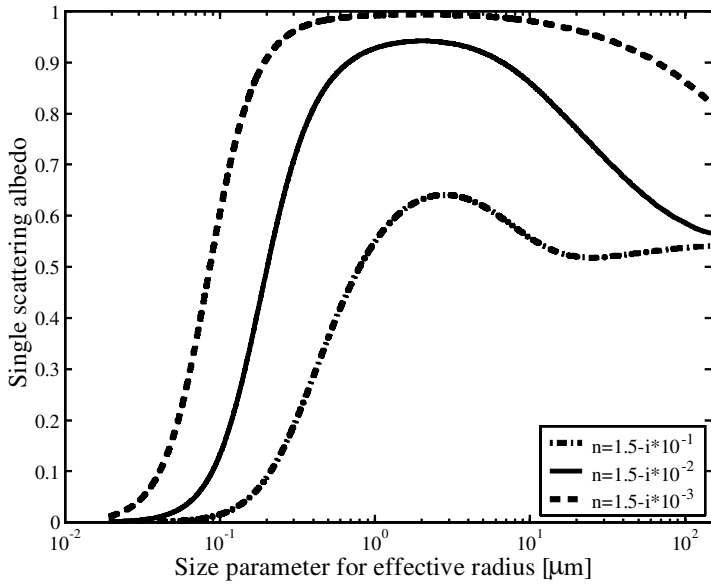


Figure 5. Single scattering albedo as a function of size parameter, based on size distribution effective radius. The dashed line corresponds to (constant with wavelength) refractive index, $n = 1.5 - i10^{-3}$, the solid line is for $n = 1.5 - i10^{-2}$, and the dash-dotted line is for $n = 1.5 - i10^{-1}$.

$k = 10^{-3}$, the solid line to $k = 10^{-2}$, and the dash-dotted line corresponds to $k = 10^{-1}$. In the IR (8–12 μm) part of the spectrum, the size parameter is usually less than $x_{\text{eff}} < 1$ and the SSA is, therefore, a strong function of the effective radius. The decrease of particle radius leads to a decrease of the SSA and a change of the surface and TOA IR aerosol forcing. Also, one can infer that small particles (fine mode) are ‘black’ in the IR and, therefore, only large particles can effectively scatter radiation.

(c) *Infrared aerosol forcing*

In this section we derive the long-wave radiative aerosol forcing at the surface and at the TOA. At the surface, the forcing is defined as the difference between downward long-wave flux with the aerosol and the flux without the aerosol. In contrast to the solar region (where the sun is the source of energy from space and even small aerosol backscatter can cause a negative aerosol forcing), the IR aerosol forcing at the surface is always positive. This is caused by the additional downward flux from the aerosol layers. At the TOA the outgoing long-wave radiation is, in most cases, decreased by the aerosols, except for strong inversion cases when the temperature of the aerosol is higher than the surface temperature. To determine the aerosol forcing, we perform radiative-transfer calculations with and without aerosols in the atmosphere.

The effect of aerosols on long-wave radiation is significant only in the atmospheric window, where the absorption by gases (mostly water vapour and carbon dioxide) is small. Therefore, we present model results in the atmospheric window range (8–12 μm). We compare these model results with the aerosol forcing obtained from detailed observations based on M-AERI FTIR spectra (Vogelmann *et al.* 2003). The M-AERI spectra contain the combined downward emissions by aerosols and greenhouse gases

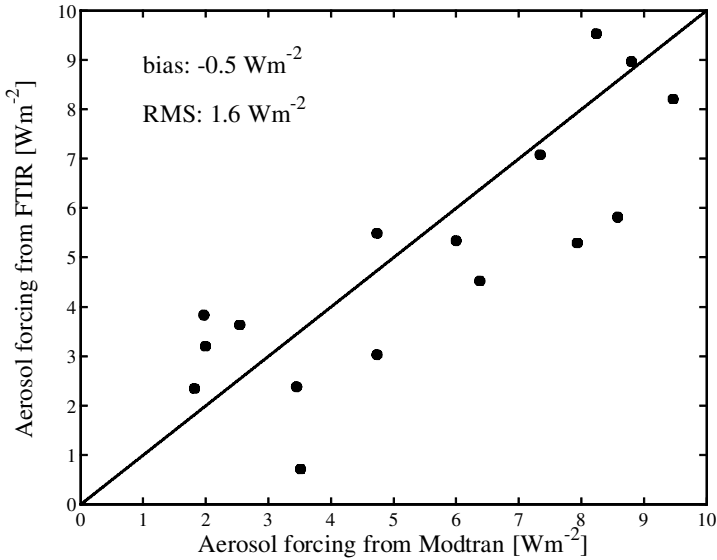


Figure 6. Comparison of long-wave aerosol forcing at the surface obtained from the radiative-transfer model, MODTRAN, and Fourier transform infrared (FTIR) observations. The solid line corresponds to perfect agreement.

(e.g. H₂O, CO₂). The aerosol's radiative effect was obtained by removing the contribution of gaseous emission using a modelled, aerosol-free spectrum. The aerosol radiance effect was converted to an aerosol IR radiative forcing using a radiance-to-flux conversion. The clean-sky spectra were computed using the Line-By-Line Radiative Transfer Model. In Vogelman *et al.* (2003) the water vapour and temperature profiles are specified every 10 minutes using M-AERI retrievals for the lowest 3 km and, above that, the nearest radiosonde launched from the ship, whereas in this work we used only the radiosonde data.

The comparison of the surface IR aerosol forcing obtained from M-AERI and from our radiative-transfer model is shown in Fig. 6. Although the mean differences between model and observations are small (0.5 W m⁻² bias), the r.m.s. is relatively large at 1.6 W m⁻². Recall that the model calculations are based on surface optical properties derived from the chemical characterization of the aerosol, and the vertical extinction profile derived from lidar and visible AOT at 500 nm. Possible discrepancies between the M-AERI and the model results reported here may be related to the fact that the surface chemistry is not representative of the lower troposphere, and that dust properties are not modelled properly. Also, the lidar extinction algorithm is a possible source of error. However, the overall comparison is good, and many temporal features are resolved by our model as illustrated in Fig. 7. This provides additional support for the aerosol optical property model. In the central part of the Pacific Ocean, the long-wave surface forcing is small and equal to about 1 W m⁻² with the exception of YD85.

For comparison, the solar aerosol forcing in this region is -5 W m⁻² (Markowicz *et al.* 2003). During YD85 the long-wave aerosol forcing increased and in the morning was about 6 W m⁻², which decreased to about 4.5 W m⁻² in the late afternoon. The mean diurnally averaged solar aerosol forcing on YD85 was -22 W m⁻². The Georgia Tech./Goddard Global Ozone Chemistry Aerosol Radiation Transport (GOCART) model (Mian Chin, private communication; results not presented) shows dust in the boundary layer for that day. This indicates that the combined effect of the sea

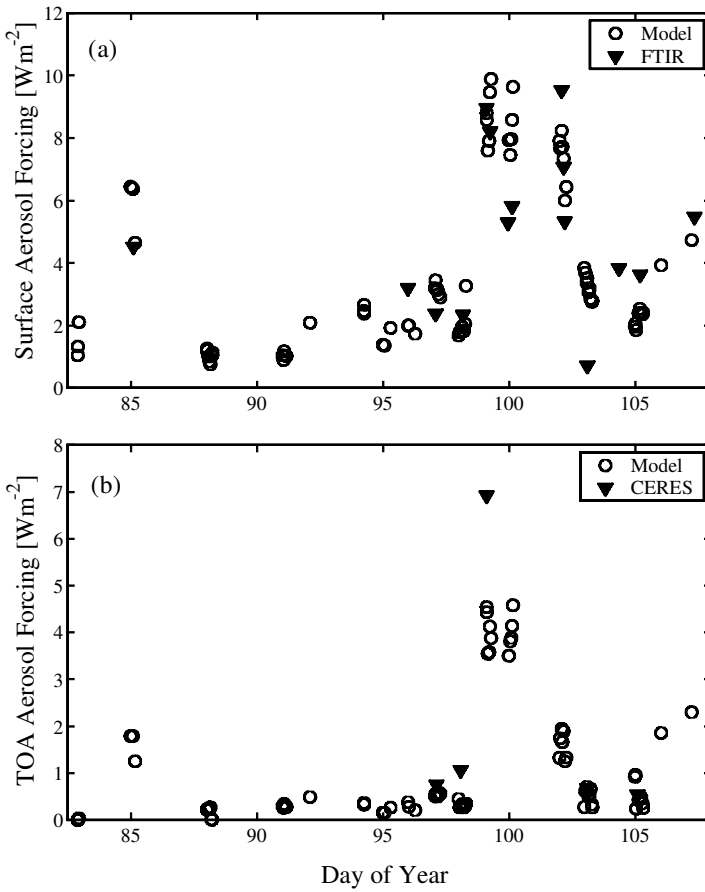


Figure 7. (a) Surface and (b) top of atmosphere (TOA) infrared aerosol forcing as a function of the year day (YD). The open circles represent radiative-transfer model results; the solid triangles in (a) define the surface forcing obtained from the Fourier transform infrared (FTIR) observations and in (b) for the TOA from the TERRA satellite CERES (Clouds and the Earth's Radiant Energy System) data. The YD99 point is misclassified by the satellite algorithm.

salt close to surface and dust in the boundary layer has an important effect on radiation in both solar and IR wavebands, leading to a strong cooling at the surface. Between YD86 and YD99 the IR forcing slowly increased to over 2 W m^{-2} . The maximum aerosol forcing observed on YD99 and YD100 (8 to 10 W m^{-2}) is associated with the dust layer in the middle troposphere. For these days the surface aerosol forcing in the solar region is about five times larger (absolute value) than in the IR forcing. The IR forcings for YD99 and YD102 are similar but their AOTs (both in solar and IR) are different. This is because on YD99 the dust was between 5 – 10 km , and on YD102 it was closer to the surface; thus, the temperature effect of the warmer dust compensated for its smaller optical depth.

The long-wave TOA aerosol forcing is obtained from the radiative-transfer model and CERES data (only five clear, collocated days). The TOA forcing is estimated by subtracting the clear (without aerosol) outgoing flux in the atmospheric window (obtained from the radiative-transfer model) from the flux measured by the CERES instrument. By plotting the IR forcing as a function of the IR AOT, we noticed a bias

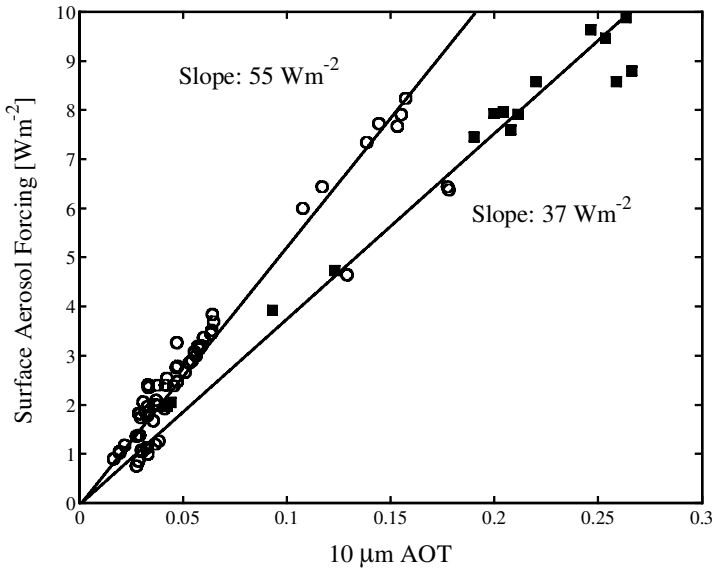


Figure 8. The long-wave aerosol forcing at the surface as function of infrared aerosol optical thickness (AOT). Squares represent aerosol forcing during the upper-layer event and open circles are for all other days. The upper-layer dust event was classified on the basis of surface and aerosol temperatures $(T_s/T_a)^4 > 1.2$ (see text).

for small AOTs of approximately 0.9 W m^{-2} . However, based on physical grounds, one would not expect any forcing for small AOTs. Such a bias may be due to several factors related to clear-sky model imperfections. Guided by the slope technique derived for the solar spectrum forcing calculations (Satheesh and Ramanathan 2000), we applied the same methodology to remove the bias. Figure 7(b) shows the temporal variation of the TOA IR aerosol forcing: the solid triangles show the aerosol forcing at the TOA between YD97 and YD105 obtained from satellite; the open circles are the model results. The results are in good agreement with radiative-transfer calculations, with the exception of YD99. During this day, the aerosol forcing from satellite observations is about 2.5 W m^{-2} larger than that obtained from the model. However, YD99 was misclassified by the satellite algorithm as cloudy, probably due to hazy conditions. The largest forcing is about 4.5 W m^{-2} during YD99 and YD100, and is about 50% of that at the surface. Much smaller TOA forcing was observed on YD102, which is due to the previously discussed temperature effect. The TOA aerosol forcing without dust is small and did not exceed 0.5 W m^{-2} . However, for the sea salt dominated YD85, the TOA long-wave forcing is between 1.2 and 1.8 W m^{-2} . The TOA IR aerosol forcing is about 15–25% of the solar TOA forcing.

The strong correlation between IR aerosol forcing at the surface and the IR ($10 \mu\text{m}$) AOT is shown in Fig. 8. This is based on the following criterion $(T_s/T_a)^4 > 1.2$, where T_s is the surface temperature and T_a is the mean aerosol temperature. It can be seen that, to a first approximation, the IR aerosol forcing is a linear function of the IR AOT. Let us define the IR aerosol forcing efficiency as the ratio of aerosol forcing to IR AOT. The IR forcing efficiency is 55 W m^{-2} (per IR optical depth unit) for the boundary-layer aerosol, and 37 W m^{-2} (per IR optical depth unit) in the case of elevated dust. If the aerosols are close to the surface, they cause an increase in the surface forcing but a decrease in the TOA forcing. The TOA aerosol forcing is shown as a function of the IR AOT in Fig. 9. The forcing efficiency is about 18 W m^{-2} (per IR optical depth

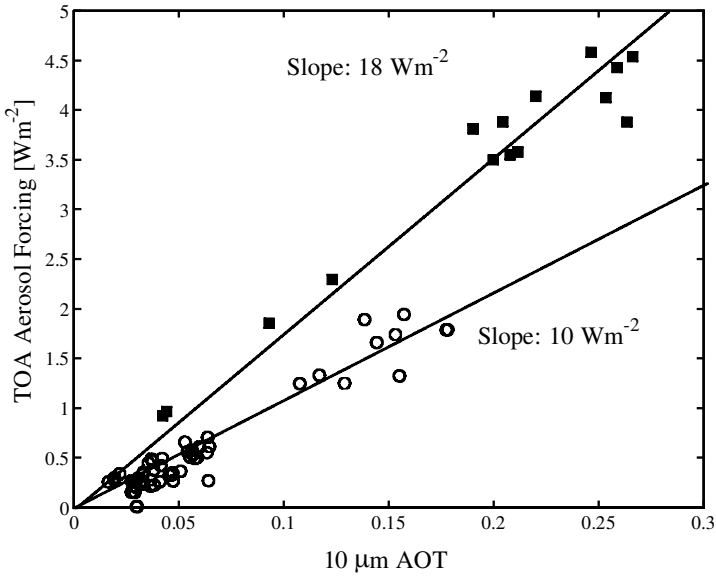


Figure 9. Same as Fig. 8 but for the top of atmosphere (TOA) aerosol forcing.

unit) in the case of elevated dust, and 10 W m^{-2} (per IR optical depth unit) when the aerosol is mostly in the boundary layer. This difference in forcing efficiency is due to the emission temperature.

We attempted to derive the radiative forcing using the Eppley broadband, hemispheric field of view pyrgeometer, but the results were unpromising. This is most probably due to several effects: (i) too broad a spectral range ($3.5\text{--}50 \mu\text{m}$); (ii) the hemispheric field of view (cloud contamination); (iii) uncertainty in the water vapour profiles.

5. A SIMPLE MODEL OF INFRARED FORCING

In this section we develop a simple two-stream model to gain insight into the physics of dust forcing. We assume that the aerosol layer is isothermal and that there is no gaseous absorption in the atmospheric window. Neglecting multiple scattering we can write the flux at the top (F_t^\uparrow) and at the bottom (F_s^\downarrow) of the aerosol layer as:

$$F_t^\uparrow = T F_s^\uparrow + F_s^\uparrow R^\uparrow + \pi A B_a, \quad (1)$$

$$F_s^\downarrow = R^\downarrow F_s^\uparrow + \pi A B_a, \quad (2)$$

where B_a is the black body irradiance at the temperature of the aerosol layer. Parameters A and T are the aerosol absorption and transmittance, R^\uparrow and R^\downarrow are up and down reflection coefficients, respectively, subscripts 's' and 'a' stand for surface and aerosol, respectively. In the case of small optical thickness τ , the parameters in (1) and (2) can be written as:

$$T = 1 - \tau, \quad (3)$$

$$A = \tau(1 - \omega), \quad (4)$$

$$R^\uparrow = \tau\omega(1 - \beta), \quad (5)$$

$$R^\downarrow = \tau\omega\beta, \quad (6)$$

where ω is a single scattering albedo and β is the backscatter coefficient. The radiative forcing above and below the aerosol layer can be written as:

$$\Delta F_t = \tau F_s^\uparrow \{(1 - B_a/B_s)(1 - \omega) + \omega\beta\}, \quad (7)$$

$$\Delta F_s = \tau F_s^\uparrow \{(B_a/B_s)(1 - \omega) + \omega\beta\}, \quad (8)$$

where B_s is the black body irradiance at the surface temperature. In this simple model the aerosol forcing at the TOA and at the surface is a linear function of the IR AOT. The first terms in (7) and (8) are associated with the thermal emission by the aerosol layer relative to the surface emission, and the second terms are associated with the downward scattered fraction of radiance. For typical values, the terms at the TOA are comparable, while at the surface the contribution by the relative emission is about two to three times larger than the scattering term. Thus, the TOA IR aerosol forcing is more sensitive to the aerosol scattering, in contrast to the surface aerosol forcing.

The thermal effects at the TOA and at the surface are opposite, and are consistent with detailed radiative-transfer model calculations (Figs. 8 and 9). The up-scattered backscatter coefficient can be written approximately as $\beta = (1 - g)/2$ (Wiscombe and Grams 1976), where g is the asymmetry parameter. The influence of the backscatter on the IR aerosol forcing is similar at the TOA and at the surface. In both cases the increase in the backscatter leads to an increase of the aerosol forcing. Thus, smaller particles (small g , but with sufficient concentrations for non-negligible extinction) have a larger influence on the aerosol forcing in the IR due to the scattering effect, which is similar to the solar aerosol forcing. The IR SSA influences the IR aerosol forcing in two opposite ways: the decrease of SSA (higher absorption) leads to an increase of the thermal emission by the aerosol layer, but to a decrease of the scattered part of radiation. It follows from (8) that for

$$\beta < B_a/B_s \quad (9)$$

the decrease of SSA leads to an increase of the IR aerosol forcing at the surface. This condition is always satisfied, because the backscatter coefficient is less than 0.5 and the ratio B_a/B_s is usually between 0.8 and 1. The SSA influence on the TOA aerosol forcing is more complicated. For

$$B_a/B_s < 1 - \beta \quad (10)$$

a decrease of SSA leads to an increase of the IR aerosol forcing at the TOA. Thus, for a constant backscatter coefficient one can always find a temperature at which the TOA aerosol forcing is increasing with increased absorption. For typical atmospheric conditions (10) may or may not be satisfied. Therefore, the relationship between the IR TOA forcing and SSA changes depends on relative black body temperatures and the backscatter coefficient. On the other hand, the short-wave TOA forcing always increases with increasing absorption (and can even change sign).

6. THE ROLE OF SCATTERING AND TOTAL WATER VAPOUR CONTENT ON TOP OF ATMOSPHERE AND SURFACE INFRARED FORCING

We can investigate the role of scattering on the IR aerosol forcing ('scattering') by keeping the total aerosol absorption and extinction constant, and performing two radiative-transfer model (MODTRAN) calculations: (a) with the asymmetry parameter set equal to unity; and (b) with the asymmetry parameter determined from the aerosol optical model. Figures 10(a) and (b) correspond to the surface and the TOA aerosol

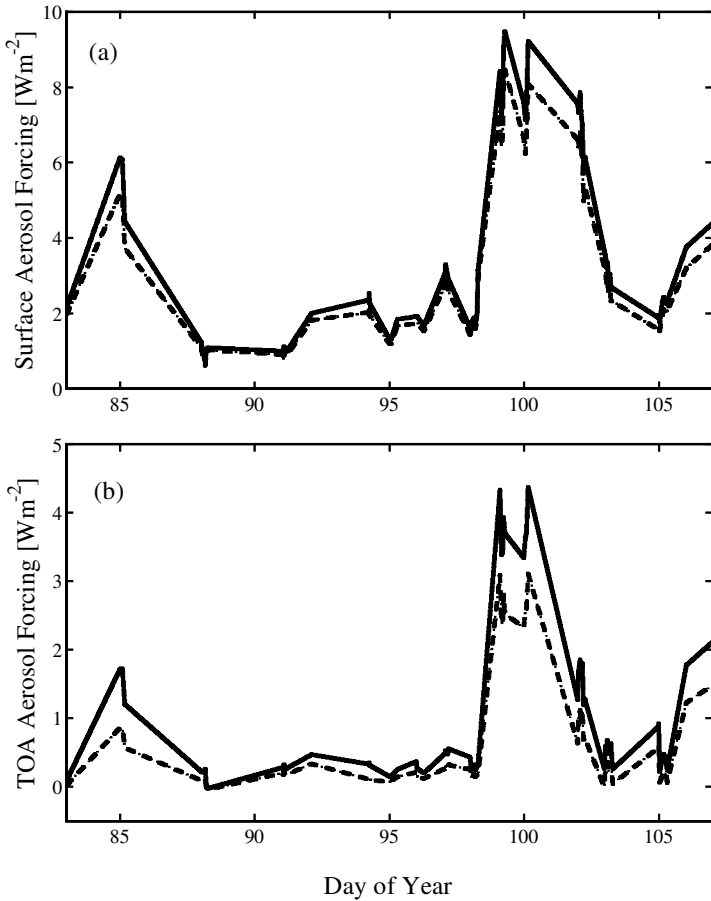


Figure 10. The aerosol infrared forcing as a function of the year day for: (a) the surface, and (b) the top of atmosphere (TOA). Computation is either exact (solid line) or neglects scattering (dotted line).

forcing, respectively. Solid lines are for g determined from the aerosol optical model and dotted lines are for $g = 1$. In the last case only forward scattering is possible.

Neglecting aerosol scattering leads to an underestimate of the surface and TOA IR forcing. Scattering has a larger effect on the TOA forcing, and this result is consistent with the simple aerosol forcing model. Neglecting scattering causes a mean error between 20 and 30%. The surface aerosol forcing decreases about 10–15% when the backscattering is set to zero. These results are consistent with the model results presented by Dufresne *et al.* (2002).

To estimate the water vapour effect on IR aerosol forcing we performed additional calculations varying the total water vapour content. Figure 11 shows the TOA and the surface aerosol forcing computed on YD99. Changing the column water vapour from 0 to 3 g cm⁻² leads to large decrease in the surface aerosol forcing by about 50%, while it is only 9% at the TOA. The relationship between the total water vapour content and the TOA and surface IR aerosol forcings is complicated, and depends on vertical profiles of water vapour and extinction coefficient. The small influence of water vapour on the IR TOA indicates that water vapour will play a secondary effect here in retrievals of the IR aerosol effects from satellite observations. On the other hand, when examining all cruise

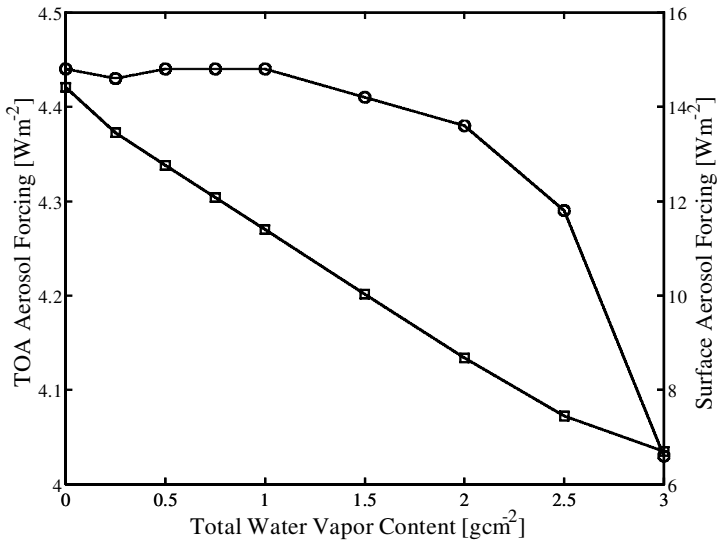


Figure 11. The top of atmosphere (TOA, open circles) and the surface (open squares) aerosol forcing as a function of the total water vapour content on year day 99.

data we did not observe a significant correlation between the long-wave surface aerosol forcing and the total column water vapour, because the optical depth and temperature provided the dominant effect.

7. CONCLUSIONS

In this paper, aerosol IR radiative forcing is studied in detail. On the basis of chemical measurements and optical properties in the visible (MPL lidar and sunphotometer observations) we estimated the IR aerosol optical thickness, single-scattering albedo, and an asymmetry parameter. The surface model results were compared to FTIR-based aerosol forcing observations by Vogelmann *et al.* (2003). The uncertainty in their method is about $\pm 1 \text{ W m}^{-2}$. The r.m.s. of the difference between the FTIR and our model calculations is about 1.6 W m^{-2} . Possible discrepancies may be related to uncertainties in the vertical representations of the chemistry, uncertainties in dust properties and refractive indices, errors in lidar extinction retrievals, and errors in the visible AOT estimates. Despite these errors, the present model properly resolves many features. We were also able to compare satellite observations for five clear, collocated days and obtained good agreement with the atmospheric-window derived forcing and the CERES satellite retrievals. This combined approach augments the FTIR observational study, tests the optical model, and thus provides the opportunity to derive IR forcing at the TOA and IR single-scattering properties.

We found that the IR AOT is strongly correlated with the IR aerosol forcing at the TOA and at the surface. The mean IR AOT at $10 \mu\text{m}$ was $0.08 (\pm 0.07)$ and SSA was 0.55. The IR aerosol forcing (all the forcing values are averaged over several measurement points during the day when the sun was visible) reaches up to 10 W m^{-2} during the ACE-Asia cruise, which is a significant contribution to the total (solar plus IR) direct aerosol effect. Figure 12 shows the mean diurnal solar (calculated every half-hour) and long-wave (averaged over several observational points) aerosol forcing at:

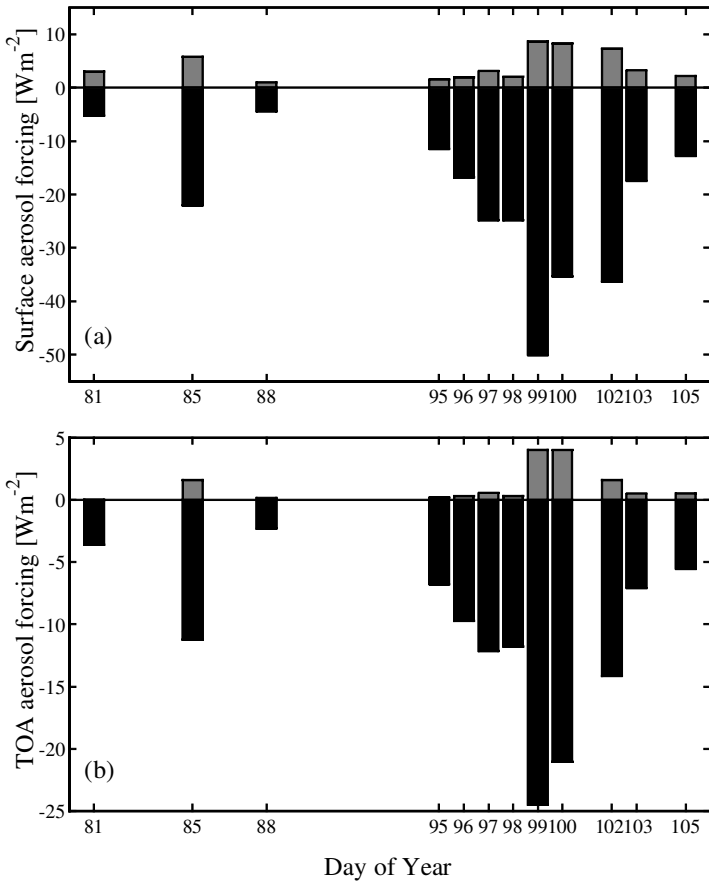


Figure 12. Comparison between (a) the surface and (b) the top of atmosphere (TOA) short-wave and infrared (IR) aerosol forcing. The positive values (grey bars) correspond to the IR forcing and negative values (black bars) are for the solar aerosol forcing.

(a) the surface, and (b) the TOA. The surface IR aerosol radiative forcing is between 10 and 25% of the short-wave aerosol forcing. The IR TOA aerosol forcing is between 1% and 19% of the solar aerosol forcing (Fig. 12(b)). Our results show that the negative solar aerosol forcing during days with large AOT (YD99, YD100, YD102) is decreased by the IR forcing by about 20%. Over the Sea of Japan the mean solar forcing during ACE-Asia was -26.1 W m^{-2} (Markowicz *et al.* 2003) and the total solar-IR radiative forcing was -21.5 W m^{-2} at the surface.

At the TOA the mean short-wave forcing was -12.7 W m^{-2} and the total was -11.2 W m^{-2} . For a constant aerosol temperature, the TOA and the surface forcing are linear functions of the IR AOT. We define the IR forcing efficiency as a useful parameter to describe the aerosol effects at the TOA and at the earth's surface. The TOA forcing efficiency is a strong function of the aerosol layer temperature, and changes between 10 and 18 W m^{-2} (per IR unit of optical depth) while the surface forcing efficiency varied between 37 and 55 W m^{-2} (per IR unit of optical depth). For comparison, the solar aerosol forcing efficiency over the Sea of Japan was -27 W m^{-2} (per 500 nm unit of optical depth) at the TOA, and -58 W m^{-2} (per 500 nm unit of optical depth) at the surface.

ACKNOWLEDGEMENTS

KMM was supported by a junior Fulbright grant. We would like to thank both referees for very comprehensive reviews. One of them was Jim Haywood who graciously provided us with copies of pre-prints related to the SHADE experiment results. PJF was supported by the National Science Foundation Climate Dynamics Program and by the ONR Program Element PE0602435N. AMV was supported by the National Science Foundation (ATM-0109135) grant. We would like to thank Joao Teixeira for his comments. Dave Bates collected lidar data during the *R/V Ronald H. Brown* cruise.

REFERENCES

- Ackerman, S. A. and Chung, H. 1992 Radiative effects of airborne dust on regional energy budgets at the top of the atmosphere. *J. Appl. Meteorol.*, **31**, 223–233
- Anderson, G. P., Berk, A., Acharya, P. K., Matthew, M. W., Bernstein, L. S., Chetwynd, J. H., Dothe, H., Adler-Golden, S. M., Ratkowski, A. J., Felde, G. W., Gardner, J. A., Hoke, M. L., Richtsmeier, S. C. and Jeong, L. S. 2001 MODTRAN4, version 2: radiative transfer modeling. *SPIE-Int. Soc. Opt. Eng.*, **4381**, 455–459
- Bates, T. S., Huebert, B. J., Gras, J. L., Griffiths, F. B. and Durkee, P. A. 1998 International Global Atmospheric Chemistry (IGAC) project's first aerosol characterization experiment (ACE 1): Overview. *J. Geophys. Res.*, **103**, 16297–16318
- Bohren, C. F. and Huffman, D. R. 1983 *Absorption and scattering of light by small particles*. J. Wiley and Sons, New York, USA
- Chylek, P., Srivastava, V., Pinnick, R. G. and Wang, R. T. 1988 Scattering of electromagnetic waves by composite spherical particles: Experiment and effective medium approximations. *Appl. Opt.*, **27**, 2396–3404
- Dufresne, J. L., Gautier, C., Ricchiazzi, P. and Fouquart, Y. 2002 Longwave scattering effects of mineral aerosols. *J. Atmos. Sci.*, **59**, 1959–1966
- Hanel, G. and Zankl, B. 1979 Aerosol size and relative humidity: Water uptake by mixture of salts. *Tellus*, **31**, 478–486
- Hess, M., Koepke, P. and Schult, I. 1998 Optical properties of aerosols and clouds: The software package OPAC. *Bull. Am. Meteorol. Soc.*, **79**, 831–844
- Highwood, E. J., Haywood, J. M., Silverstone, M. D., Newman, S. M. and Taylor, J. P. 2003 Radiative properties and direct effect of Saharan dust measured by the C-130 aircraft during SHADE.2: Terrestrial spectrum. *J. Geophys. Res.*, in press
- Hobbs, P. V. 1999 An overview of the University of Washington airborne measurements and results from the Tropospheric Aerosol Radiative Forcing Observational Experiment (TARFOX). *J. Geophys. Res.*, **104**, 2233–2238
- Hsu, N. C., Herman, J. R. and Weaver C. J. 2000 Determination of radiative forcing of Saharan dust using combined TOMS and ERBE data. *J. Geophys. Res.*, **105**, 20649–20661
- IPCC 2001 'Climate change 2001: The scientific basis'. Contribution of Working Group I to the third assessment report of the Intergovernmental Panel on Climate Change. Ed. J. T. Houghton. Cambridge University Press, Cambridge, UK
- Kaufman, Y. J., Hobbs, P. V., Kirchoff, V., Artaxo, P., Remer, L. A., Holben, B. N., King, M. D., Ward, D. E., Prins, E. M., Longo, K. M., Mattos, L. F., Nobre, C. A., Spinhime, J. D., Ji, Q., Thompson, A. M., Gleason, J. F., Christopher, S. A. and Tsay, S. C. 1998 Smoke, Clouds, and Radiation—Brazil (SCAR-B) experiment. *J. Geophys. Res.*, **103**, 31783–31808

- Lelieveld, J., Berresheim, H., Borrmann, S., Crutzen, P. J., Dentener, F. J., Fischer, H., Feichter, J., Flatau, P. J., Heland, J., Holzinger, R., Kormann, R., Lawrence, M. G., Levin, Z., Markowicz, K. M., Mihalopoulos, N., Minikin, A., Ramanathan, V., de Reus, M., Roelofs, G. J., Scheeren, H. A., Sciare, J., Schlager, H., Schultz, M., Siegmund, P., Steil, B., Stephanou, E. G., Stier, P., Traub, M., Warneke, C., Williams, J. and Ziereis, H. 2002 Global air pollution crossroads over the Mediterranean. *Science*, **298**, 794–799
- Loeb, N. G. and Kato, S. 2002 Top-of-atmosphere direct radiative effect of aerosols over the tropical oceans from the Clouds and the Earth's Radiant Energy System (CERES) satellite instrument. *J. Climate*, **15**, 1474–1484
- Lubin, D. and Simpson, A. S. 1994 The longwave emission signature of urban pollution: radiometric FTIR measurement. *Geophys. Res. Lett.*, **21**, 37–40
- Lubin, D., Satheesh, S. K., McFarquhar, G. and Heymsfield, A. J. 2002 Longwave radiative forcing of Indian Ocean tropospheric aerosol. *J. Geophys. Res.*, **107**, doi: 10.1029/2001JD001183
- Malm, W. C., Sisler, J. F., Huffman, D., Eldred, R. A. and Cahill, T. A. 1994 Spatial and seasonal trends in particle concentration and optical extinction in the United States. *J. Geophys. Res.*, **99**, 1347–1370
- Markowicz, K. M., Flatau, P. J., Quinn, P. K., Carrico, C. M., Flatau, M. K., Vogelmann, A. M. and Liu, M. 2003 Influence of relative humidity on aerosol radiative forcing. *J. Geophys. Res.*, **108**, in press
- Morys, M., Mims, F. M., Hagerup, S., Anderson, S. E., Baker, A., Kia, J. and Walkup, T. 2001 Design, calibration, and performance of the MICROTOPS II handheld ozone monitor and Sun photometer. *J. Geophys. Res.*, **106**, 14573–14582
- Myhre, G. and Stordal, F. 2001 Global sensitivity experiments on the radiative forcing due to mineral aerosols. *J. Geophys. Res.*, **106**, 18193–18204
- Quinn, P. K., Coffman, D. J., Bates, T. S., Miller, T. L., Johnson, J. E., Voss, K., Welton, E. J. and Neususs, C. 2001 Dominant aerosol chemical components and their contribution to extinction during the Aerosols99 cruise across the Atlantic. *J. Geophys. Res.*, **106**, 20783–20809
- Quinn, P. K., Coffman, D. J., Bates, T. S., Miller, T. L., Johnson, J. E., Welton, E. J., Neususs, C., Miller, M. and Sheridan, P. J. 2002 Aerosol optical properties during INDOEX 1999: Means, variability, and controlling factors. *J. Geophys. Res.*, **107**, 8020, doi:10.1029/2000JD000037
- Raes, F., Bates, T., McGovern, F. and Van Liedekerke, M. 2000 The 2nd Aerosol Characterization Experiment (ACE-2): general overview and main results. *Tellus*, **52**, 111–125
- Ramanathan, V., Crutzen, P. J., Lelieveld, J., Mitra, A. P., Althausen, D., Anderson, J., Andreae, M. O., Cantrell, W., Cass, G. R., Chung, C. E., Clarke, A. D., Coakley, J. A., Collins, W. D., Conant, W. C., Dulac, F., Heintzenberg, J., Heymsfield, A. J., Holben, B., Howell, S., Hudson, J., Jayaraman, A., Kiehl, J. T., Krishnamurti, T. N., Lubin, D., McFarquhar, G., Novakov, T., Ogren, J. A., Podgorny, I. A., Prather, K., Priestley, K., Prospero, J. A., Quinn, P. K., Rajeev, K., Rasch, P.,

- Rupert, S., Sadourny, R.,
Satheesh, S. K., Shaw, G. E.,
Sheridan, P. and
Valerol, V. P. J.
- Revercomb, H. E., Buijs, H., 1988 Radiometric calibration of IR Fourier transform spectrometers: solution to a problem with the High Resolution Interferometer Sounder. *Appl. Opt.*, **27**, 3210–3218
- Rothman, L. S., Rinsland, C. P., 1998 The HITRAN molecular spectroscopic database and HAWKS (HITRAN Atmospheric Workstation): 1996 edition. *J. Quant. Spectrosc. Radiat. Transfer*, **60**, 665–710
- Goldman, A., Massie, S. T.,
Edwards, D. P., Flaud, J. M.,
Perrin, A., CamyPeyret, C.,
Dana, V., Mandin, J. Y.,
Schroeder, J., McCann, A.,
Gamache, R. R.,
Wattson, R. B., Yoshino, K.,
Chance, K. V., Jucks, K. W.,
Brown, L. R., Nemtchinov, V.
and Varanasi, P.
- Satheesh, S. K. and Ramanathan, V. 2000 Large differences in tropical aerosol forcing at the top of the atmosphere and earth's surface. *Nature*, **405**, 60–63
- Sokolik, I. N., Toon, O. B. and 1998 Modeling the radiative characteristics of airborne mineral aerosols at infrared wavelengths. *J. Geophys. Res.*, **103**, 8813–8826
- Bergstrom, R. W.
- Spänkuch, D., Dohler, W. and 2000 Effect of coarse biogenic aerosol on downwelling infrared flux at the surface. *J. Geophys. Res.*, **105**, 17341–17350
- Guldner, J.
- Swap, R. J., Annegarn, H. J. and 2002 The Southern African Regional Science Initiative (SAFARI 2000): Summary of science plan. *South African J. Sci.*, **98**, 119–124
- Otter, L.
- Tegen, I., Lacis, A. A. and Fung, I. 1996 The influence on climate forcing of mineral aerosols from disturbed soils. *Nature*, **380**, 419–422
- Turpin, B. J. and Lim, H. J. 2001 Species contributions to PM_{2.5} mass concentrations: Revisiting common assumptions for estimating organic mass. *Aerosol Sci. Technol.*, **35**, 602–610
- Vogelmann, A. M., Flatau, P. J., 2003 Observations of large aerosol infrared forcing at the surface. *Geophys. Res. Lett.*, **30**(12), 1655, doi: 10.1029/2002GL016829
- Szczodrak, M.,
Markowicz, K. M. and
Minnett, P. J.
- Welton, E. J., Voss, K. J., 2000 Ground-based lidar measurements of aerosols during ACE-2: Instrument description, results, and comparisons with other ground-based and airborne measurements. *Tellus*, **52**, 636–651
- Gordon, H. R., Maring, H.,
Smirnov, A., Holben, B.,
Schmid, B., Livingston, J. M.,
Russell, P. B., Durkee, P. A.,
Formenti, P. and
Andreae, M. O.
- Wiscombe, W. J. and Grams, G. W. 1976 The backscattered fraction in two-stream approximations. *J. Atmos. Sci.*, **33**, 2440–2451